RESEARCH ARTICLE

CARBON ENERGY WILEY

Highly N-doped carbon with low graphitic-N content as anode material for enhanced initial Coulombic efficiency of lithium-ion batteries

Yihua Tang[1,2] 🟢 | Jingjing Chen[3] | Zhiyong Mao[3] | Christina Roth[1] |
Dajian Wang[3]

[1]Department of Electrochemical Process Engineering, Universität Bayreuth, Bayreuth, Germany

[2]Chair of Electrochemical Process Engineering, Bavarian Center for Battery Technology (BayBatt), Bayreuth, Germany

[3]Tianjin Key Laboratory for Photoelectric Materials and Devices, School of Materials Science and Engineering, Tianjin University of Technology, Tianjin, PR China

Correspondence
Yihua Tang, Department of Electrochemical Process Engineering, Universität Bayreuth, Universitätsstraße 30, 95447 Bayreuth, Germany.
Email: Yihua.Tang@uni-bayreuth.de

Abstract

N-doped carbons as one of the most prominent anode materials to replace standard graphite exhibit outstanding Li^+ storage performance. However, N-doped carbon anodes still suffer from low N-doping levels and low initial Coulombic efficiency (ICE). In this study, high N-doped and low graphitic-N carbons (LGNCs) with enhanced ICE were synthesized by taking advantage of a denitrification strategy for graphitic carbon nitride (g-C_3N_4). In brief, more than 14.5 at% of N from g-C_3N_4 (55.1 at% N) was retained by reacting graphitic-N with lithium, which was subsequently removed. As graphitic-N is largely responsible for the irreversible capacity, the anode's performance was significantly increased. Compared to general N-doped carbons with high graphitic-N proportion (>50%) and low N content (<15 at%), LGNCs delivered a low proportion of 10.8%–17.2% within the high N-doping content of 14.5–42.7 at%, leading to an enhanced specific capacity of 1499.9 mAh g^{-1} at an ICE of 93.7% for the optimal sample of LGNC (4:1). This study provides a facile strategy to control the N content and speciation, achieving both high Li^+ storage capacity and high ICE, and thus promoting research and application of N-doped carbon materials.

KEYWORDS
denitrification, graphitic carbon nitride, graphitic-N, lithium-ion batteries, N-doped carbon

1 | INTRODUCTION

As the most widely used energy storage devices, lithium-ion batteries (LIBs) demonstrate favorable features, such as high energy density, high working voltage, rechargeability, low self-discharge, and so forth. While LIBs consist of cathode, anode, electrolyte, and separator, the anode attracted significant attention in current research.

Carbon anode materials are eco-friendly, conductive, abundant, and stable, but their theoretical capacity of 372 mAh g^{-1} is too low to fulfill the ever-growing demands from electrical vehicles, drones, and smart grids. So far, strategies focus on developing completely new anode materials (e.g., silicon, tin, lithium titanate) and sophisticated structural design (e.g., nanotube, graphene, heteroatom doping) as well as composite

formation (e.g., coating, sandwiching) to enhance electrochemical properties of LIB anodes.

Heteroatom doping is an effective technique to modify and improve the performance of carbons since among others it increases their capacity, lowers the diffusion barrier for Li^+ intercalation, and boosts their wettability.[1] Nitrogen is a neighbor of carbon in the periodic table, its very similar physicochemical properties should allow for a facile doping into the carbon lattice. Consequently, it is the most widely used dopant to modify the electronic and chemical properties of carbons.[2] For example, Zhu et al.[3] presented a self-templating strategy and postacid-etching treatment to prepare both N and O codoped carbon delivering a reversible discharge capacity as high as $1121.8 \, \text{mAh g}^{-1}$ at $0.1 \, \text{A g}^{-1}$ for LIBs. Yan et al.[4] demonstrated that heteroatoms (S, N) could reduce the diffusion barrier for Li^+ in LIBs significantly. Yu et al.[5] reported that N-doping can effectively improve the wettability of the interface between the carbon and electrolyte, and thereby the electrochemical performance could be enhanced. Zhang et al.[6] utilized the N-doped carbon-derived synergistic effect to achieve superior structural stability and boosted Li^+ transportation, and the prepared core-shell ZnTe@N-doped carbon nanowires delivered high specific capacity and advanced rate performance. Gomez-Martin et al.[7] showed an electrochemical evaluation of N-doped carbons as anodes for LIBs and demonstrated that higher N-doping levels lead to an improved rate capability and specific capacity, whereas they result in a decreased energy efficiency. The high irreversible capacity of the electrode would lead to a short lifetime and even pose a risk for safe operation.[8,9] N-doped carbons have been researched continuously in recent years, but there still exist three striking knowledge gaps: (i) How to increase the N-doping level of N-doped carbons further? (ii) Why is the initial Coulombic efficiency (ICE) so low for N-doped carbons? (iii) How to control the N species being formed?

Previously, the classical N-doping method included either postdoping or in situ doping strategies; however, it has been very difficult to reach >15 at% of N content.[10,11] Consequently, we would like to introduce a novel "denitrification" strategy to prepare highly N-doped carbons derived from graphitic carbon nitride ($g\text{-}C_3N_4$), which has a honeycomb-like lattice formed of tri-s-triazine and an ultrahigh N content of 55.1 at%. In earlier theoretical studies, $g\text{-}C_3N_4$ was recognized as a potential anode material for LIBs, for example, Pan et al.[12] simulated the electrochemical properties of $g\text{-}C_3N_4$, and pointed out that $g\text{-}C_3N_4$ could have a specific capacity as high as $1165.3 \, \text{mAh g}^{-1}$. In practice, however, $g\text{-}C_3N_4$ exhibits poor Li^+ storage performance due to its poor conductivity and high initial irreversible capacity attributed to the irreversible reaction between Li^+ and bridged N in $g\text{-}C_3N_4$.[13] To overcome both issues, we have first developed a so-called "denitrification" strategy to prepare high N-doped carbons (N content reaches up to 33.7 at%) derived from $g\text{-}C_3N_4$ by using Mg, Zn, and polyvinyl pyrrolidone (PVP).[14–16] These $g\text{-}C_3N_4$-derived carbons exhibited both high N content and good capacity, but still also featured comparatively low ICE (<50%).

Based on the results from our previous research and most of the literature from other researchers,[12–18] we agree with the hypothesis that graphitic-N is responsible for the low ICE. Veith et al.[13] reported a solid lithiation method and pointed out that the graphitic-N would irreversibly react with Li^+ to result in irreversible capacity. Hankel et al.[18] performed density functional theory calculations showing that the pyrrolic-N and pyridinic-N would enhance the electrochemical performance of N-doped carbons, whereas graphitic-N would only lead to poor cycling stability and low performance. All these three kinds of N species have sp^2 hybrid orbitals, but their structures and properties are very different from each other. It is noteworthy that pyridinic-N has two lone pair electrons, pyrollic-N has a special π^6_5 conjugated system, and graphitic-N provides the last valence electron to the antibonding orbital. As a result, pyrollic-N and pyridinic-N could transform into graphitic-N during carbonization, and graphitic-N can only be removed by a denitrification step. The irreversible reaction of graphitic-N with lithium is parasitic and detrimental, but it also gives us a chance to selectively capture the graphitic-N by using lithium.

Based on the denitrification, herein we turned the unfavorable reaction between lithium and graphitic-N into an advantage to prepare the low graphitic-N carbons (LGNC) within a high N-doping level. During the denitrification and carbonization, the graphitic-N would irreversibly react with lithium to form an undefined compound, which is subsequently leached and removed. By reverse engineering and explicitly facilitating the reaction between graphitic-N and lithium, LGNC showing enhanced ICE and exceptional Li^+ storage capacity were prepared. Furthermore, structural characterization and electrochemical tests have been performed to investigate the structure, morphology, and electrochemical properties of LGNC. The N-doping level of LGNC was tuned from 42.7 to 14.5 at%, combined with an improved ICE reaching up to 95.6% and an optimal Li^+ storage capacity of $1499.9 \, \text{mAh g}^{-1}$. We hope this study will not only promote research in N-doped carbons but also provide a dialectic approach toward more sophisticated materials modification.

2 | METHODS

2.1 | Samples preparation

LGNC were synthesized by using g-C_3N_4 as a precursor, and lithium metal powder (Shanghai Oujin Lithium Industrial Co., Ltd.) as both reductant and prelithiation reagent. The g-C_3N_4 precursor was prepared by thermal polycondensation of melamine (Shanghai Aladdin Biochemical Technology Co., Ltd.). Typically, ~50 g melamine was loaded into an alumina crucible with a cover and then put into a muffle furnace, followed by being heated up to 550°C at a ramp rate of 10°C min^{-1} and held in the atmosphere for 3 h. In an argon-filled glove box, a 5 g mixture with different weight ratios of g-C_3N_4/lithium metal powder (g-C_3N_4: Li = 2:1, 4:1, and 8:1) was almost filling the 10 mL molybdenum crucible with a lid, and then manually stirred for 10 min, followed by an annealing step at 650°C, 750°C, or 850°C with a ramping rate of 10°C min^{-1} and 2 h preservation under 50 mL min^{-1} argon-flow in a tube furnace inside of the glove box; then the mixture was naturally cooled to room temperature. To remove the residual Li and inactive undefined Li compound, the resulting product was washed with deionized water and ethanol three times, followed by vacuum drying to obtain the final LGNC.

2.2 | Sample characterization

Powder X-ray diffraction (XRD) patterns of samples were recorded on an AR EQUINOX 3000 X (Thermo Fisher Scientific) with Cu Kα1 radiation ($\lambda = 1.54,056$ Å). Fourier-transform infrared (FTIR) spectra of samples mixed with KBr were recorded on a Nicolet iS10 (Thermo Fisher Scientific). Raman spectra of samples were recorded on a HORIBA EVOLUTION laser Raman spectrometer (HORIBA JOBIN YVON S.A.S.) with a He–Ne laser (532 nm) as the excitation source. For g-C_3N_4, the Raman spectra were also excited by a Bruker RAM II module with an Nd:YAG laser ($\lambda = 1064$ nm) scanning a range from 200 to 3500 cm^{-1} and a resolution of 4 cm^{-1}. X-ray photoelectron spectroscopy (XPS) data were collected on an Escalab 250 Xi (Thermo Fisher Scientific). Quanta FEG 250 (FEI) scanning electron microscope (SEM) was carried out to reveal the morphologies of the different samples. Transmission electron microscope (TEM) images and high-resolution transmission electron microscope (HRTEM) images were recorded on a Talos F200X (FEI) TEM coupled with an energy dispersive spectrometer (EDS; Oxford Instrument). The electrical conductivities of the samples were measured on an ST2722-SZ four-probe resistivity tester (Suzhou Jingge Electronic Co.), the sample was loaded into a slot and the pillar containing the probe applied pressure of 3–20 Mpa on the topside of the sample, and then the conductivities were recorded automatically. The nitrogen adsorption–desorption isotherms were recorded at 77 K on a BEL-Max analyzer (BEL) to reveal the specific surface area and porous structure of the samples, and the isotherms were analyzed by using BEL-Master™ 7.

2.3 | Electrochemical measurement

The electrochemical Li$^+$ storage properties of LGNC were investigated in CR2025 coin-type LIBs, which were assembled in an argon-filled glove box. The assembling process refers to our previous work.[16] Typically, the working electrode slurry was prepared by mixing LGNC, acetylene black, and polyvinylidene fluoride in 8:1:1 (wt/wt/wt) in the solvent of N-methyl-2-pyrrolidone. Then, the slurry was cast onto a copper foil current collector with a 100 μm wet film, followed by vacuum drying at 80°C for 12 h, with a painting rate of 20 cm min^{-1}. The dried film was compressed at 10 MPa and was punched into working electrodes (areal mass loading of ~0.5 mg cm^{-2}), lithium disks of 12 mm diameter were used as both reference electrode and counter electrode, 1 M lithium hexafluorophosphate dissolved in a 1:1 (vol/vol) mixture of ethylene carbonate and dimethyl carbonate was used as the electrolyte, and microporous polypropylene film (Celgard 2400) was employed as the separator.

Cyclic voltammetry (CV) was performed with a potential window of 0–3.0 V (vs. Li/Li$^+$) under a series scan rate of 0.1, 0.2, 0.5, 1, 2, and 5 mV s^{-1} on a CHI760E (CH Instruments) electrochemical workstation. Electrochemical impedance spectroscopy (EIS) was performed in a frequency range of 100 kHz–10 mHz with an AC signal of 5 mV amplitude as the perturbation; also, the EIS was performed on the CHI760E electrochemical workstation. Galvanostatic cycling test was performed with a current density of 0.05 A g^{-1}; meanwhile, rate performance was evaluated at 0.05, 0.1, 0.2, 0.5, 1, 2, and 5 A g^{-1} on an automatic battery tester system (Land CT2001A) with a working voltage window of 0.01–3 V (vs. Li/Li$^+$). The galvanostatic intermittent titration technique (GITT) was also performed with stabilized cells after 20 cycles, with a 15 min pulse current of 0.05 A g^{-1} following a relaxation time of 15 min.

3 | RESULTS AND DISCUSSION

XRD was performed to investigate the structure of the synthesized g-C_3N_4 precursor and the synthesized LGNC. As shown in Figure 1A, g-C_3N_4 shows two characteristic
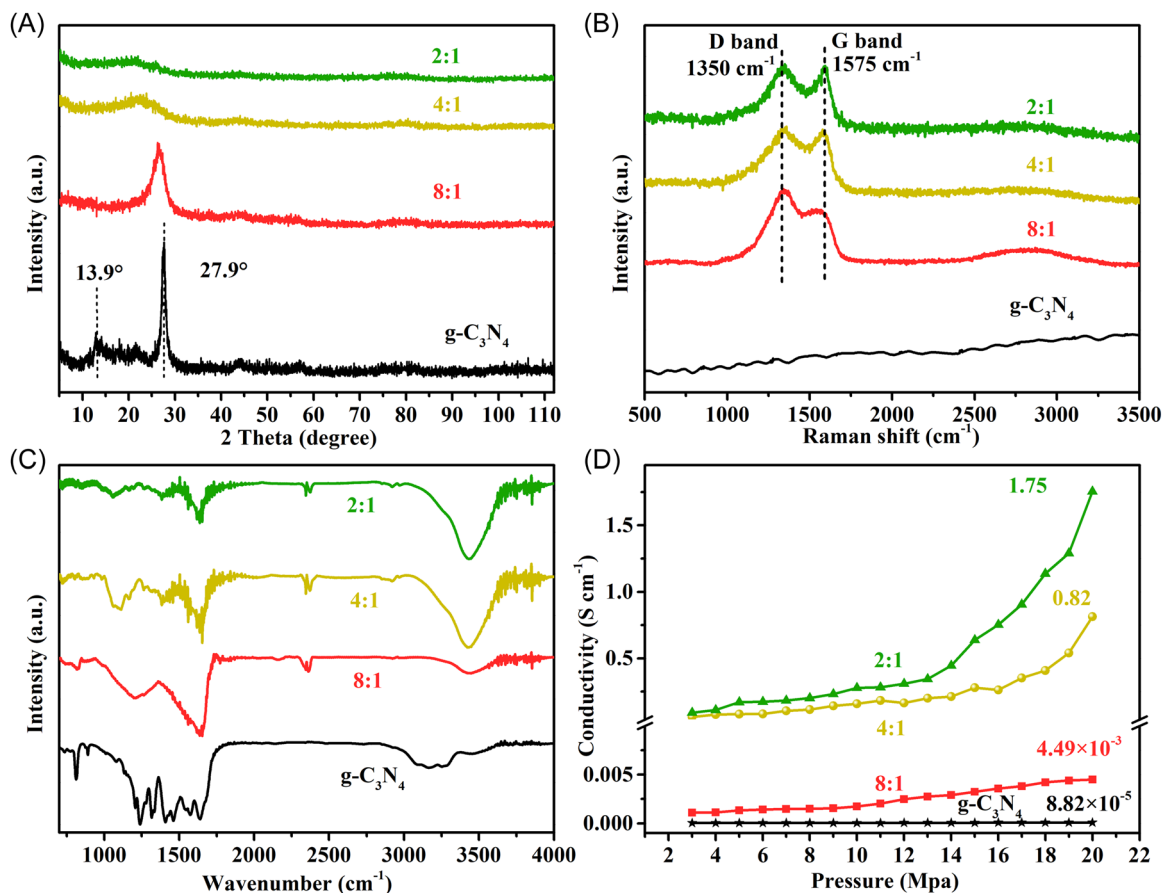
FIGURE 1 (A) XRD patterns, (B) Raman spectra, (C) FTIR, and (D) electronic conductivities for pristine g-C_3N_4 and LGNC. FTIR, Fourier-transform infrared spectroscopy; LGNC, low graphitic-N carbon; XRD, X-ray diffraction.

reflections located at ~13.9° which are assigned ~27.9° and assigned to the (100) and (002) planes, respectively. In the transformation step, Li would react with graphitic-N and thereby disturb the structure of g-C_3N_4. In agreement with this, for LGNC with mass ratio of 8:1 (g-C_3N_4:Li), a reduced peak at ~27.9° was observed, supporting the theory of g-C_3N_4 structural collapse. For LGNC at ratios 4:1 and 2:1, the characteristic broad peak located at ~22.5° was comparable to the reflection of amorphous carbon, revealing the high degree of amorphous carbon in LGNC. Then, Raman spectra were recorded and analyzed to evaluate the structure of LGNC, as shown in Figure 1B. No significant Raman signal was observed on pristine g-C_3N_4 (because of the fluorescence effect), but two clear Raman peaks were revealed on LGNC. The peaks located at ~1350 and ~1575 cm^{-1} were assigned to the characteristic D (=disordered) band and G (=graphitic) band corresponding to breathing vibration and stretching vibration belonging to amorphous carbon, respectively.[19] Generally, the D and G bands indicate structure defect and graphitization degree, respectively. The I_D/I_G band intensity ratios were calculated to be 1.21 (8:1), 1.03 (4:1), and 1.01 (2:1), clearly indicating an increase in the defect level of LGNC with increasing g-C_3N_4 amount.[20] The Raman spectra

of g-C_3N_4 under 1064 nm laser have also been detected, as shown in Figure S1. Raman peaks observed at ~707, ~980, and ~1236 cm^{-1} are assigned to the breathing modes of s-triazine, which is present in the g-C_3N_4.[21] To further investigate the structure of g-C_3N_4 and LGNC, FTIR spectra were recorded, as shown in Figure 1C. g-C_3N_4 exhibited vibration peaks at ~810 cm^{-1} corresponding to the triazine group, and peaks at ~1100–1800 cm^{-1} corresponding to the vibration of CN aromatic heterocycles. For LGNC, there were peaks at ~1250 cm^{-1} corresponding to C–N and peaks at ~1600 cm^{-1} corresponding to C=N, indicating the transformation of tri-s-triazine into N-doped carbons.[22] Noteworthy, LGNC at 8:1 showed indistinct peaks at ~810 cm^{-1} corresponding to deformed triazine groups, which corroborates the incomplete carbonization, being in agreement with XRD and Raman results. As shown in Figure 1D, electronic conductivities were detected by a four-probe tester. g-C_3N_4 is a semiconductor with a poor conductivity of 8.82×10^{-5} S cm^{-1} at 20 MPa, whereas LGNC demonstrated significantly enhanced conductivities of 4.49×10^{-3}, 0.82, and 1.75 S cm^{-1} for LGNC 8:1, 4:1, and 2:1, respectively. The electronic conductivity was boosted with an increase of the Li portion within the starting

material and attributed to the higher carbonization degree. From the above analysis, we suggest that the ratio of Li metal within the precursor significantly affects the carbonization and denitrification in this study, and LGNC with 8:1 ratio showed intermediate features between g-C_3N_4 and carbons. Besides composition, the influence of the annealing temperature was also investigated. As shown in Figure S2A–D, the LGNC of 4:1 was heated at 650°C, 750°C, and 850°C to present the effect of the annealing temperature. The XRD board peak of amorphous carbon became insensitive and shifted to higher degrees as the annealing temperature increased, and the I_D/I_G band intensity ratios decreased from 1.18 (650°C) to 1.03 (750°C) and to 0.87 (850°C), and the electric conductivity increased from 0.01 S cm^{-1} (650°C) to 0.82 S cm^{-1} (750°C) and to 3.22 S cm^{-1} (850°C). Thus, the carbonization degree was increased by this treatment, whereas the defect level was decreased with an increase in annealing temperature; this is in agreement with our previous work.[15] Generally, the carbonization degree is inversely related to the N proportion, whereas the defect level and electronic conductivity increase with N content.[23,24] According to the above characterizations, we concluded that the precursor g-C_3N_4 could be transformed into N-doped carbons gradually with the reduction of Li metal powder, and the N content probably declines with an increasing Li content within the precursor or the annealing temperature. We deduced that the Li would react with graphitic-N first to deform the tri-*s*-triazine structure of g-C_3N_4, and then the deformed tri-*s*-triazine fragments would start to transform into the graphitic honeycomb structure under a higher temperature of 650°C, 750°C, and 850°C, and the carbonization degree would increase when the temperature goes up. Then the residue of inactive undefined Li compound can be removed by water and ethanol in the washing process.

SEM and TEM were employed to characterize the morphology of LGNC. As shown in Figure 2A–C, LGNC at 8:1 exhibits a potholes morphology with a few pieces similar to g-C_3N_4 (Figure S3A–D), and LGNC at 4:1 has a more fragmented structure with abundant pores and slits. In contrast, LGNC at 2:1 has a more laminated structure with more pores and slits, and wrinkled morphology. Qualitatively, the specific surface area and porosity should increase with increasing Li proportion of the precursor. Micromorphology and microstructure of the LGNC at 4:1, which has an optimal electrochemical performance (see below), have been further revealed by TEM and HRTEM images presented in Figure 2D–F. LGNC exhibits a defective layered structure with wrinkled morphology, and the interplanar distance was measured to be ~0.44 nm, which is much larger than the 0.34 nm of graphite. The enlarged interplanar distance is

favorable for Li$^+$ diffusion and storage, leading to a promoted rate performance and higher specific capacity. At the same time, EDS was performed to investigate the distribution of C and N in LGNC at 4:1. As depicted in Figure 2G–I, the obvious layered structure of LGNC was detected with C and N uniformly distributed. The porous structure provides abundant paths and shortcuts for Li$^+$ diffusion, while the enlarged surface area could reduce the actual areal current density and polarization. The TEM images of g-C_3N_4 and LGNC at 2:1 and 8:1 are provided in the Figure S3C–F. All the g-C_3N_4 and LGNC at 2:1 and 8:1 were sheet-like structures, and the wrinkling increased with the proportion of lithium metal powder in the precursor.

N_2 adsorption–desorption isotherms were conducted to quantify the specific surface area and porosity. As demonstrated in Figure 3A, all curves presented are conformal with type-IV isotherm of IUPAC classification, indicating a porous system with capillary condensation.[25] The isotherm rose rapidly due to the strong interaction between N_2 and LGNC in the low-pressure region, and then rose only gently due to the occurrence of multilayer adsorption of N_2 on the LGNC surface. Then the isotherm increased rapidly again due to capillary condensation. Besides, the observed type-H3 hysteresis loops evidenced the porous structure with slits, cracks, and wedges, which is in good agreement with the SEM images.[25] By employing brunauer-emmett-teller (BET) theory, the specific surface area was calculated to be ~79.6 m^2 g^{-1} (g-C_3N_4), ~103.2 m^2 g^{-1} (8:1), ~286.8 m^2 g^{-1} (4:1), and ~391.3 m^2 g^{-1} (2:1). By employing the non-local density functional theory model, the specific porous volume was simulated to be ~0.23 cm^3 g^{-1} (g-C_3N_4), 0.39 cm^3 g^{-1} (8:1), 2.95 cm^3 g^{-1} (4:1), and 3.14 cm^3 g^{-1} (2:1), and the pore distributions were presented in Figure 3B. The denitrification process causes the wrinkling of the sheet-liked structure, resulting in porous structures. Obviously, the degree of denitrification is proportional to the volume of the microporous and mesopores, the higher the degree of denitrification the larger the microporous/mesoporous volume. For carbon anode materials, the micropores can provide a large specific surface area to construct an electric double layer, and the mesopores are favorable for ion conduction. Thus, the LGNC were expected to present a good rate of performance. Both specific surface area and porosity were enlarged with increasing Li proportion of the precursor, indicating that Li could not only deform the lattice of g-C_3N_4 but also affect the resulting microstructure of g-C_3N_4. In general, both porous structure and enlarged surface area can lead to better chemical wettability, higher Li$^+$ diffusion coefficient, and higher surface-controlled capacity.[26] Additionally, the N_2 adsorption–desorption isothermal curves and pore distributions of the precursor (4:1) annealed at different
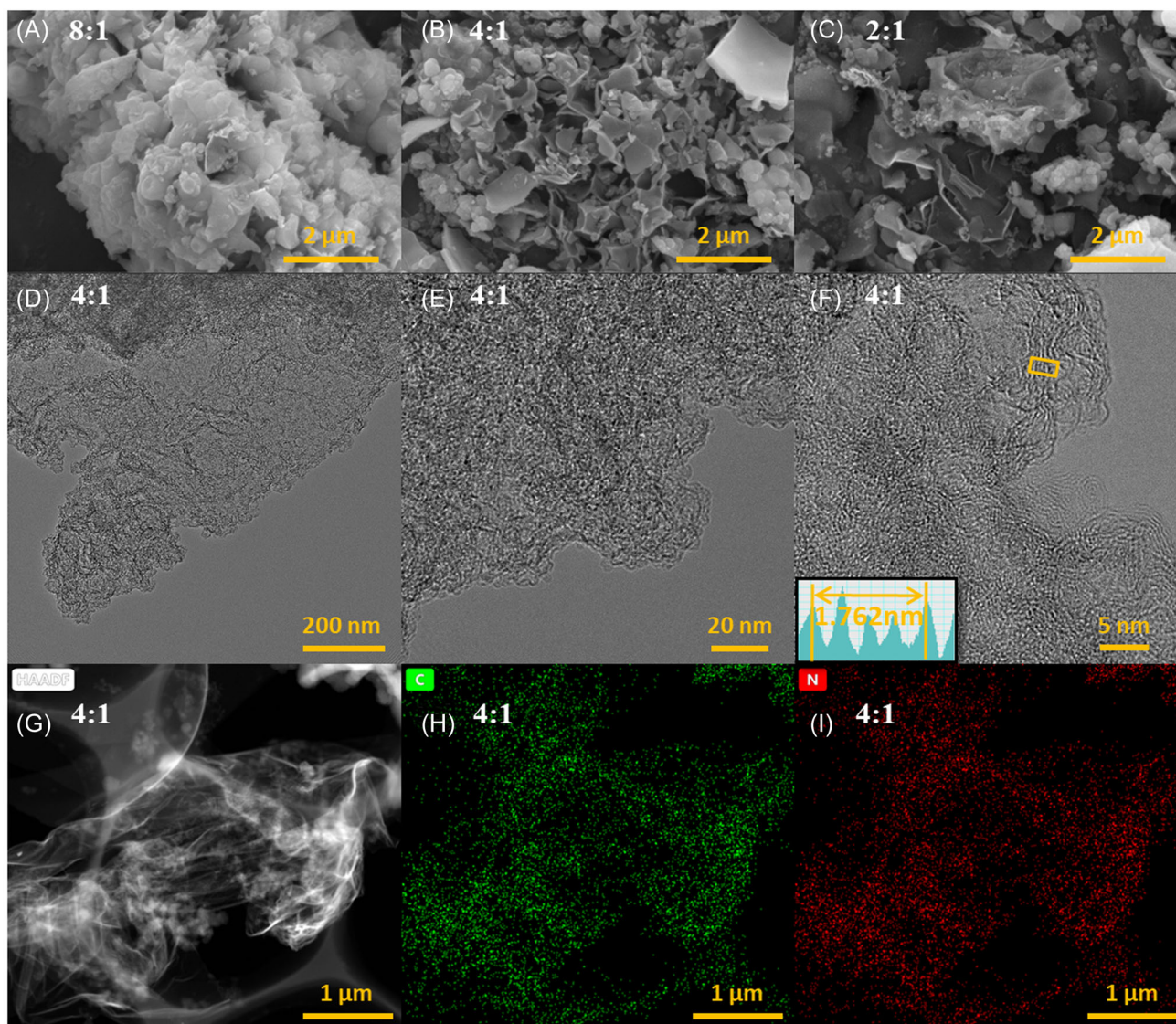
FIGURE 2 SEM images for LGNC at (A) 8:1, (B) 4:1, and (C) 2:1. (D,E) TEM images, (F) HRTEM image, (G) HAADF image, (H) C-EDS elemental mapping, and (I) N-EDS elemental mapping for LGNC at 4:1. EDS, energy-dispersive spectrometer; HAADF, high-angle annular dark-field; HRTEM, high-resolution transmission electron microscope; LGNC, low graphitic-N carbon; SEM, scanning electron microscope; TEM, transmission electron microscope.
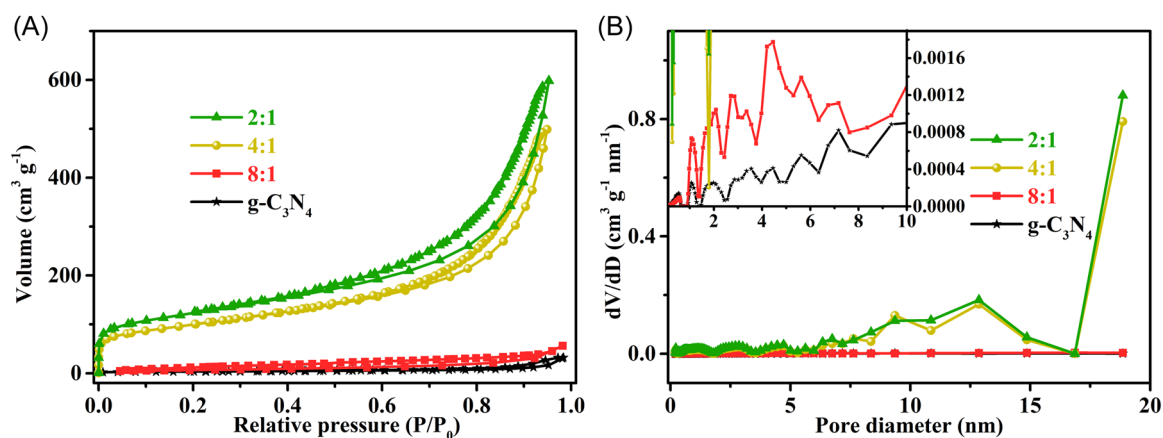
FIGURE 3 (A) N_2 adsorption–desorption isotherms and (B) pore size distribution for g-C_3N_4 and LGNC. LGNC, low graphitic-N carbon.

temperatures have been presented in the Figure S4A,B, indicating that the specific surface area and porosity increase with an increase in annealing temperature.

The chemical composition and various N species of g-C$_3$N$_4$ and LGNC were studied using XPS. Figure 4A depicts the survey XPS of g-C$_3$N$_4$ and LGNC; g-C$_3$N$_4$ has two peaks at ~285 and ~399 eV assigned to C 1s and N 1s, respectively. Apart from C and N, LGNC show two additional peaks at ~55 and ~530 eV, demonstrating the presence of Li and O. The total contents of C, N, O, and Li were calculated and listed in Table 1. It was observed that the relative amount of N 1s was reduced from 55.1 to 14.5 at % with increasing Li amount of the precursor, whereas the C 1s signal was increased from 43.7 to 67.5 at%, indicating that the N/C ratio could be tuned by tuning the Li/g-C$_3$N$_4$ ratio. Additionally, the O signal present in the spectra was attributed to the washing process and residual air in the tube furnace during annealing. High-resolution spectra of C 1s, N 1s, and Li 1s were recorded to further elucidate the chemical oxidation states of C, N, and Li. As illustrated in Figure 4B, the C 1s signal was deconvoluted into C–C/C=C at ~284.6 eV, C–O at ~285.9 eV, and N–C=N at ~288.1 eV. After Li thermal reduction, the signal of C–C/C=C was

obviously enhanced, whereas the signal of N–C=N was reduced, verifying the transformation from g-C$_3$N$_4$ to N-doped carbon. The N 1s peak was deconvoluted into pyridinic-N at ~398.1 eV, pyrrolic-N at ~399.9, and graphitic-N at ~401.2 eV for g-C$_3$N$_4$, and peaks of Li–N at ~397.6 eV for LGNC emerged (Figure 4C). The individual contributions were fitted and listed in Table 1. The g-C$_3$N$_4$ mainly consisted of pyridinic-N (41.6 at%), but g-C$_3$N$_4$ has poor Li$^+$ storage performance due to the structure collapse caused by a destructive reaction between Li$^+$ and graphitic-N (even though the graphitic-N was just 6.5 at%). Similar to g-C$_3$N$_4$, g-C$_3$N$_4$-derived LGNC has a low content of graphitic-N of 4.6, 2.8, and 2.5 at% for LGNC at 8:1, 4:1, and 2:1, respectively. This fitting result directly supports our hypothesis that graphitic-N reacts irreversibly and is leached and washed away, supporting the outstanding electrochemical performance of LGNC. As mentioned in the introduction, it has been widely recognized that pyridinic-N and pyrrolic-N could promote the facile lithiation/delithiation, but graphitic-N would be destroyed during the lithiation. The high-resolution Li 1s signals of LGNC were converted into intercalated Li at ~54.9 eV, Li$_2$CO$_3$ at ~55.8 eV, and Li–N at ~56.2 eV (Figure 4D).
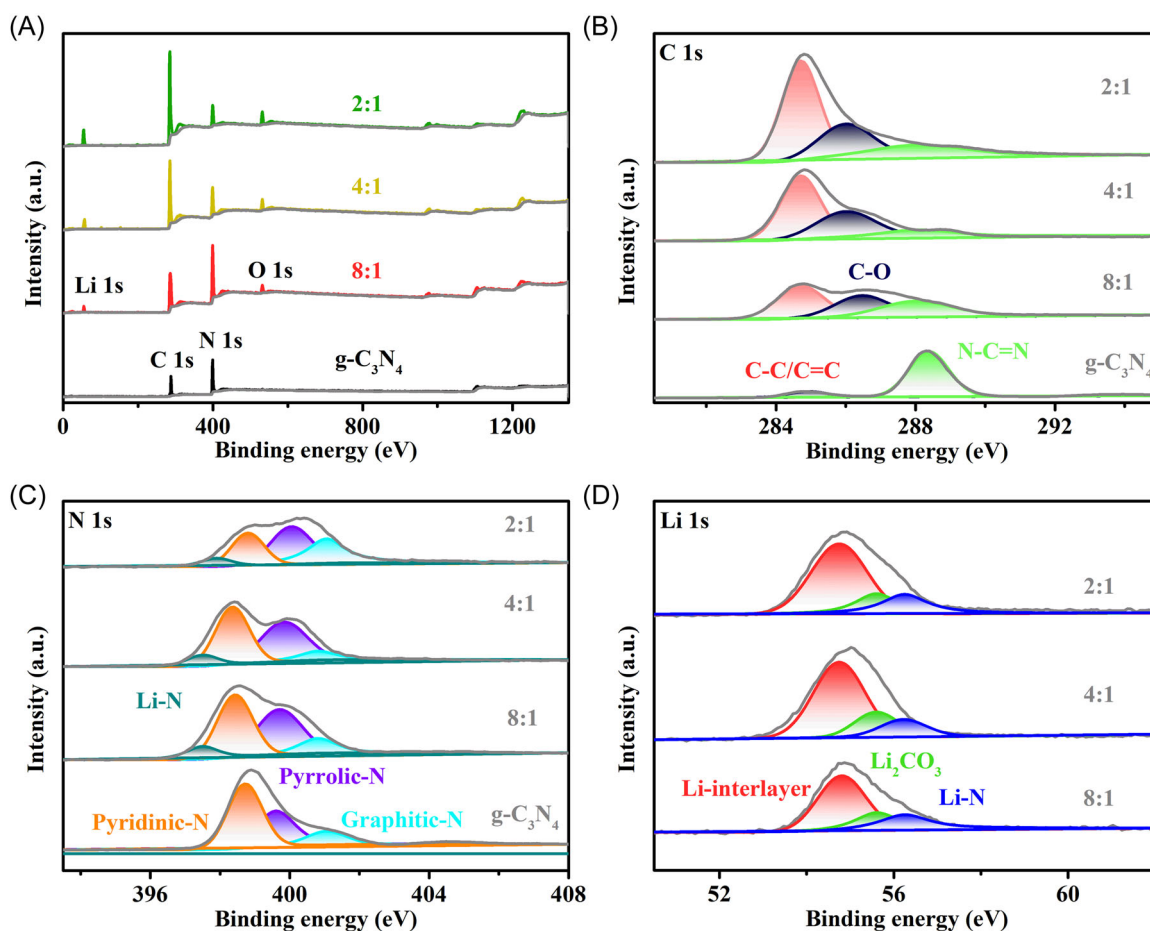

FIGURE 4 (A) XPS survey spectra and high-resolution spectra for (B) C 1s, (C) N 1s, and (D) Li 1s. XPS, X-ray photoelectron spectroscopy.

TABLE 1 Elemental composition and N configuration for g-C$_3$N$_4$ and LGNC (at%)

| Samples	C	N	O	Li	Li-N	Pyridinic-N	Pyrrolic-N	Graphitic-N
g-C$_3$N$_4$	43.7	55.1	1.2	0	0	41.6	7.12	6.5
8:1	45.2	42.7	6.5	5.6	3.1	19.9	15.1	4.6
4:1	62.2	23.1	7.3	7.4	1.9	9.8	8.6	2.8
2:1	67.5	14.5	8.4	9.6	1.4	5.1	5.5	2.5

Abbreviation: LGNC, low graphitic-N carbon.

Because of the reactivity of the Li compound formed during reaction with Li, it was not possible to transfer the material after annealing (before washing) from the tube furnace to various instruments for its systematic characterization, so all the characterization in this paper is for the final LGNC. The residual inactive Li compound did not contain much Li after the washing step, and most of the residual Li was stored in the interlayer of LGNC. By using XPS, the N species have been analyzed in detail, facilitating our in-depth understanding of the physicochemical properties of LGNC and their electrochemical behavior, as well as directly verifying the success of our strategy for removing graphitic-N.

The electrochemical performance of LGNC was measured by galvanostatic discharge/charge cycling. Figure 5A demonstrates the outstanding Li$^+$ storage capacity and good cycling stability for LGNC. At a current density of 0.05 A g^{-1}, LGNC delivered first discharge capacities of 134.1, 1759.7, and 1224.4 mAh g^{-1} for LGNC at 8:1, 4:1, and 2:1, respectively. After 100 cycles, the retained discharge capacities were 23.6 mAh g^{-1} (8:1), 1499 mAh g^{-1} (4:1), and 1022.4 mAh g^{-1} (2:1). Because of the incomplete transformation of g-C$_3$N$_4$, the LGNC at 8:1 presented poor performance and low ICE. The LGNC at 4:1 and 2:1 exhibited stable amorphous carbon structure for lithiation/delithiation, and consequently delivered enhanced capacities and stabilities. N heteroatoms affect the electrochemical performance significantly, and the LGNC at 4:1 has higher pyridinic-N and pyrrolic-N content and lower graphitic-N content than the LGNC at 2:1, so the LGNC at 4:1 offers the optimal capacity. The cycling performance of LGNC (4:1) annealed at different temperatures has been given in the Figure S5C, revealing the optimal annealing temperature of 750°C. We suggest that the carbonization was incomplete under 650°C, whereas the N content was too low under 850°C. The initial discharge/charge profiles for LGNC were plotted in Figure 5B to reveal the electrochemical reaction and ICE of samples. In the sloping discharge profile, the high voltage region (>1.5 V) is related to surface storage behavior, whereas the middle voltage region (0.5–1.5 V) is related to defects and pore storage behavior, and the low voltage region (<0.5 V) is attributed to interplanar storage

behavior.[27] Therefore, the defects and pores provide a considerable amount of capacity that is much higher than 372 mAh g^{-1} of graphite anode. The LGNC at 8:1 has a relatively low carbonization degree, so it showed a relatively low ICE of 55.9%. With the carbonization and reduction in graphitic-N, LGNC at 4:1 and 2:1 reached a competitive ICE of 93.7% and 95.6% in the carbonate electrolyte, respectively. Table 2 presents the LIB performance of some heteroatom-doped carbon materials with carbonate electrolyte, which shows that LGNC has a competitive ICE. Rate performances were tested under a series of current densities of 0.05, 0.1, 0.2, 0.5, 1, 2, 5, and back to 0.05 A g^{-1}. As shown in Figure 5C, LGNC at 4:1 and 2:1 delivered good rate performances due to their high N content and stable structure. At such a series of current densities, the LGNC at 4:1 exhibited a stable capacity of 1651, 1556, 1372, 1190, 999, 854, 654, and 1326 mAh g^{-1}. Besides, the long cycling performances of LGNC at 5 A g^{-1} have been recorded, as shown in the Figure S6. To further investigate the electrochemical process during discharging and charging, CV tests of LGNC at 4:1 were carried out with a scan rate of 0.1 mV s^{-1} (Figure 5D). In the first lithiation process, reduction peaks at ~0.8–1.2 V were assigned to the reaction between Li$^+$ and defects/pores, reduction peaks at ~0.55 V were assigned to the formation of solid electrolyte interphase (SEI) film due to the side reactions, and reduction peaks at ~0.1 V were attributed to the intercalation of Li$^+$ into the interlayer spacing.[27,28] Alternating to the anodic scan, oxidation peaks at ~0.25 V were assigned to the deintercalation of Li$^+$ from the interlayer, peaks at ~1.2 V were attributed to the extraction of Li$^+$ from defects and pores, and some minor peaks at ~1.5–2.5 V were attributed to the desorption of Li$^+$ from the electrode surface.[27,28] The difference between the first cycle and second cycle indicates that the irreversible capacity was mainly attributed to SEI formation and irreversible defects/pores with strong absorbability for electrolytes. The CV curves for LGNC derived from the 8:1 and 2:1 are given in the Figure S5A,B; LGNC (2:1) and LGNC (4:1) have a similar shape indicating similar lithiation/delithiation processes, whereas LGNC (8:1) showed a "capacitive" curve indicating the poor intercalation capacity. Figure 5E presents Nyquist plots of LGNC to
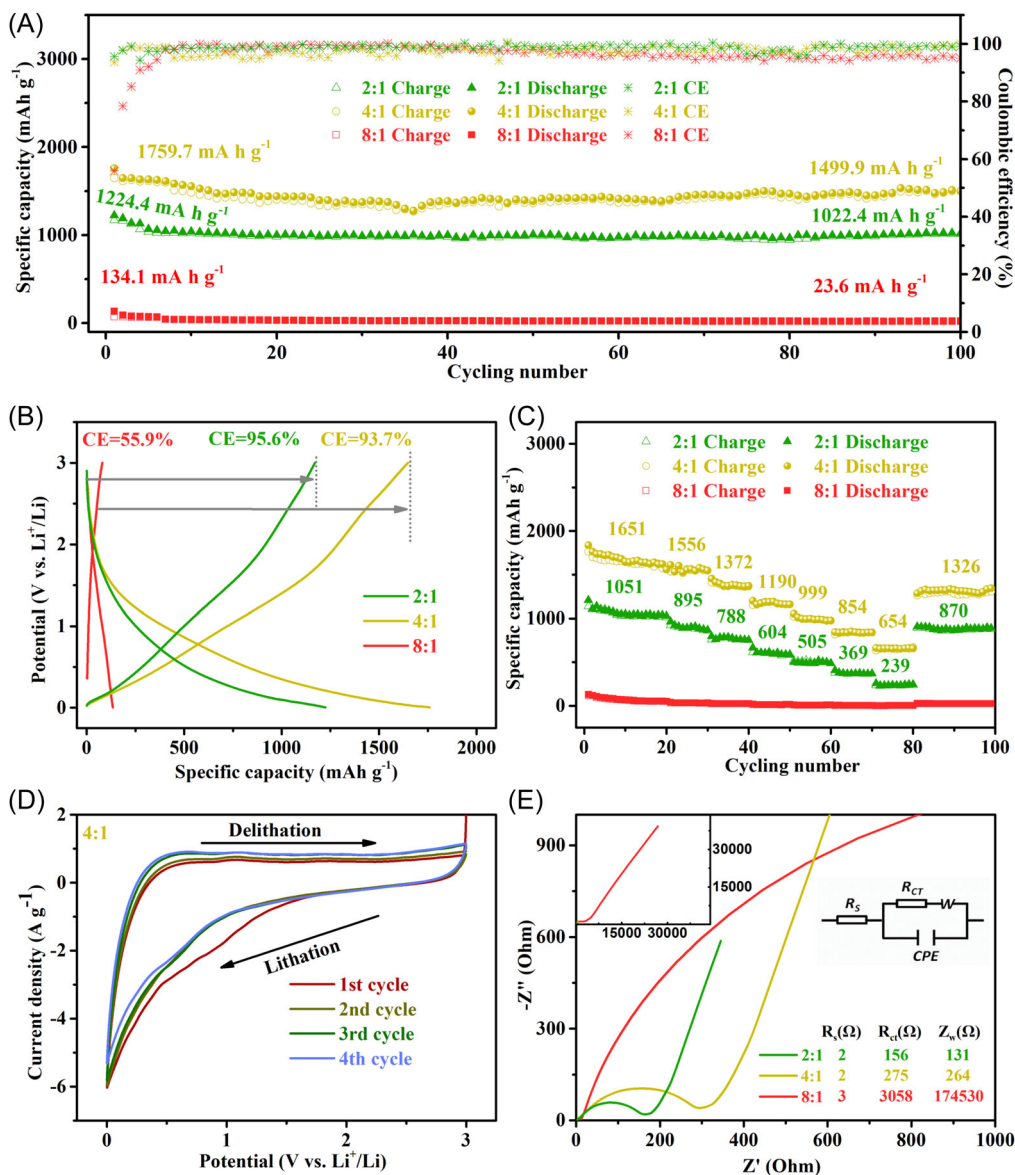
FIGURE 5 (A) Galvanostatic charge/discharge cycling performances, (B) discharge/charge profiles, and (C) rate performances for LGNC. (D) CV curves for LGNC at 4:1. (E) EIS (Nyquist) for LGNC. CV, cyclic voltammetry; EIS, electrochemical impedance spectroscopy; LGNC, low graphitic-N carbon.

understand the electrochemical impedance of electrodes. Plots for all samples are composed of a sloping line in the low-frequency region related to inductive resistance (Warburg type resistance [Z_w]) and a semicircle in the high-frequency region relating to charge transfer resistance (R_{ct}), and the intercept of the semicircle on the X-axis is assigned to the inherent resistance (R_s) of other parts, including electrolyte, separator, and so on.[29] In agreement with our expectations, the impedance decreased with the increase of Li amount in the precursor. Then we calculated the Z_w, R_{ct}, and R_s by fitting the inserted equivalent circuit. The Z_w was calculated to be 17.45 kΩ (8:1), 264 Ω (4:1), and 131 Ω (2:1), while the R_{ct} of electrodes was decreased from 3058 to 275 and to 176 Ω with the ratio of g-C$_3$N$_4$: Li changed from

8:1 to 4:1 and to 2:1, respectively. This is in good agreement with the carbonization degree and electronic conductivity discussed previously.

The Li$^+$ diffusion coefficients were further measured using GITT (Figure S5D). Typically, the Li$^+$ diffusion coefficient could be determined by using the following equation[53,54]:

$$D = \frac{4}{\pi\tau}\left(\frac{m_a V_a}{M_a A}\right)^2\left(\frac{\Delta E_d}{\Delta E_\tau}\right)^2, \quad (1)$$

therein, τ is the duration of the discharge pulse, m_a is the active mateial loading mass for the electrode, M_a is the molar mass of the active material, V_a is the compacted

TABLE 2 Summary and comparison of capacity and ICE of heteroatoms doped carbons application in LIBs using carbonate electrolyte. ICE, initial Coulombic efficiency; LIBs, lithium ion batteries

Material	Capacity (mAh g^{-1})	Cycles	Current (A g^{-1})	ICE (%)	Ref.
NPGM	496	200	0.4	58	[30]
NPG-650	900	150	0.07	55.3	[31]
CNFWs	943	600	2	48.4	[32]
NPCNFs	1150	50	0.05	59	[33]
SPC	783	100	0.15	60.6	[34]
UCMSs-600	503	100	0.05	63.5	[35]
I-doped graphene	1565	200	0.1	26.5	[36]
NP-CNSs	760	100	0.2	59.3	[37]
N-CBCNT@rP	834.3	2000	2	87.5	[38]
BC–PANI_AC	433	200	0.37	52.7	[39]
NP-BC	1846.8	50	0.1	49	[40]
NPGC-3	914	100	0.1	62.1	[41]
N-doped graphene	500	150	0.2	66.9	[42]
N-C	890	100	0.1	51	[43]
C3/C5 composite	785	800	0.45	42	[44]
N-P-C	570	200	0.1	48.5	[45]
C$_3$N$_4$-Cu	1500	240	0.1	65	[27]
BNC	300.9	100	0.1	48.3	[46]
NC-P0.2	1640	200	0.05	42	[47]
NPC-2D	488	100	0.1	62.8	[48]
NS-C	880	700	0.1	69	[49]
N-GCNs	1236	100	0.1	53.4	[50]
B-CN	195.1	100	0.1	16	[51]
NPC	1781	500	0.1	49.2	[52]
NG-750	1162	1000	1	76.6	[15]
NHCS-800	1064.5	400	0.1	84.1	[16]
LGNC (4:1)	1499.9	100	0.05	93.7	This study

Abbreviations: ICE, initial Coulombic efficiency; LIB, lithium-ion battery.

molar volume of the active material, A is the active area of the anode, ΔE_d is the voltage change during the relaxation, and ΔE_τ is the voltage change during the pulse. LGNC showed competitive Li$^+$ diffusion coefficient as a carbon material. Based on the calculation results as shown in Figure 6A, the samples with higher N content exhibited a higher Li$^+$ diffusion coefficient in most regions of the discharge/charge curve. In the discharge (lithiation) branch, the Li$^+$ diffusion coefficients of LGNC decreased with the decrease of voltage, but the discrepancy was getting smaller in the low voltage region of <0.25 V, indicating the negligible effect of N content on Li$^+$ intercalation diffusion. However, in the deintercalation process, samples with higher N content exhibited much higher Li$^+$ deintercalation diffusion. To have a better understanding of the lithiation process, we differentiated the CV curves of LGNC. As shown in Figure 6B, the differential of LGNC derived from the starting of 2:1 and 4:1 presented two peaks at ~1.25 and ~0.2 V assigned to the considerable surface absorption/adsorption and the dominant intercalation of lithium, respectively. In contrast, the differential of the 8:1 specimen indicated a strong surface absorption/adsorption as well as no intercalation reactions due to its
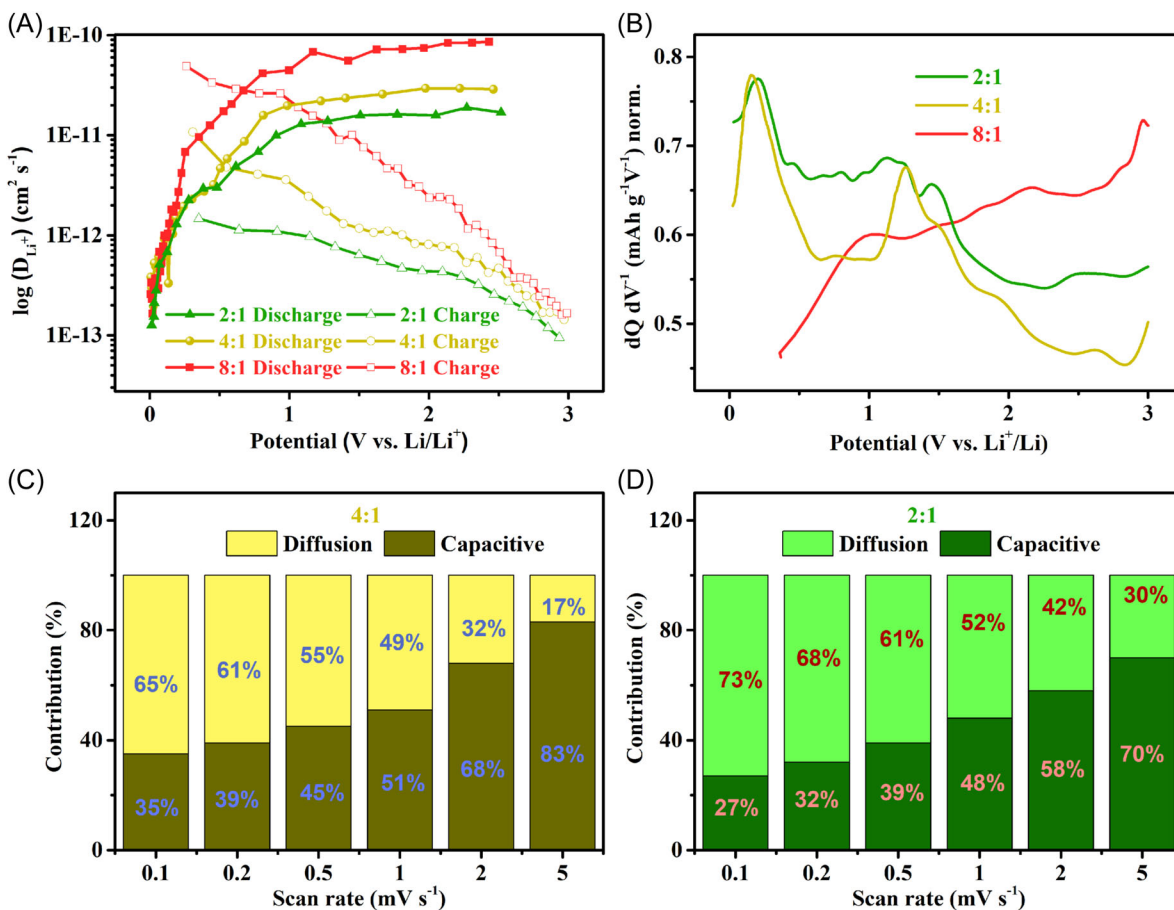
FIGURE 6 (A) Li$^+$ diffusion coefficient for LGNC. (B) Normalized differential profile of discharge/charge profile for LGNC at 4:1 and 2:1. The contribution of capacitive and diffusion-controlled capacity for LGNC at (C) 4:1 and (D) 2:1. LGNC, low graphitic-N carbon.

low carbonization degree. To reveal the influence of surface storage, CVs of LGNC derived from 2:1 and 4:1, which have obvious surface storage and intercalation behaviors, have been measured with the different scan rates of 0.1, 0.2, 0.5, 1, 2, and 5 mV/s, as shown in the Figure S7A,B. The hybrid storage could be qualitatively distinguished by resolving the b value in the following equation[53,55]:

$$i = av^b. \tag{2}$$

Therein, i is the redox peak current, v is the scan rate, and a and b are constants. In the case of diffusion behavior, the redox peak current (i) varies with the 0.5 power of the scan rate (v), whereas i varies linearly with v, suggesting a surface-controlled capacitive behavior for the electrode.[56] By fitting i couple with different v, as shown in Figure S7C,D, the values of b could be resolved to be 0.82/0.67 and 0.73/0.66 for LGNC derived from 4:1 and 2:1, respectively, indicating a mixed diffusion capacity and capacitive capacity. The contributions of

each mechanism have been evaluated by using the following equation[55]:

$$i(V) = k_1 v^{1/2} + k_2 v. \tag{3}$$

In a hybrid storage system, we could divide the current density $i(V)$ into a diffusion-controlled part ($k_1 v^{1/2}$) and a capacitive part ($k_2 v$). Each part could be determined by integrating the corresponding current density. Figure 6C,D presents the contributions of diffusion (intercalation) and capacitive (surface-controlled) of LGNC under different scan rates. The contribution of capacitive capacity was considerable and increased with the increase of scan rate, as well as supported the promising rate performance and cyclability of LGNC.

Apparently, these pre-eminent electrochemical performances come from the modified physicochemical properties of LGNC. By N-doping, LGNC exhibits abundant Li$^+$ storage sites and enlarged interplanar spacing, as well as an activated surface, benefitting the electrochemical performance. On the other hand, the

weakness of low ICE has been largely remedied by reducing the content of unfavorable graphitic-N. Overall, LGNC exhibited competitive electrochemical performance compared with other N-doped carbons.

4 | CONCLUSION

In summary, high N-doped carbons with low graphitic-N ratio have been prepared by using the denitrification and the reaction between lithium and graphitic-N. The physicochemical properties of LGNC could be modified by changing the ratio of g-C_3N_4/Li and annealing temperature. After carbonization, the tri-s-triazine structure of g-C_3N_4 transformed into the honeycomb structure of LGNC, which was stable during lithiation/delithiation. The morphology of LGNC was fragmented and porous, and the large surface area and porous structure decreased the polarization during charging/discharging. The reduction of graphitic-N has been verified by XPS analysis, in agreement with the increased ICE. Several electrochemical tests revealed the advantages of high N-doping and low graphitic-N content. The optimal two samples with 4:1 and 2:1 ratios presented the exceptional capacity of 1022.4 and 1499.9 mAh g^{-1} respectively coupled with the ICE of 95.6% and 93.7%, respectively. Besides the promising capacity and ICE, they also showed exciting rate performances and cycling stability. All these advantages could be attributed to the N-doping and reduction of graphitic-N. By taking the feature of the unfavorable reaction, this study interpreted that weakness might be a special advantage in disguise. This innovative preparation demonstrated the simultaneous realization of high N-doping and low graphitic-N content for promising Li$^+$ storage performance and promoted the development and application of N-doped carbons.

CONFLICTS OF INTEREST
The authors declare no conflicts of interest.

ORCID
Yihua Tang http://orcid.org/0000-0003-3754-5293

REFERENCES

1. Radinger H, Hartmann M, Ast M, et al. Understanding efficient phosphorus-functionalization of graphite for vanadium flow batteries. *Electrochim Acta*. 2022;409:139971.

2. Wu JX, Cao YL, Zhao HM, Mao JF, Guo ZP. The critical role of carbon in marrying silicon and graphite anodes for high-energy lithium-ion batteries. *Carbon Energy*. 2019;1(1): 57-76.

3. Zhu L, Zhang Z, Luo J, Zhang H, Qu Y, Yang Z. Self-templated synthesis of hollow hierarchical porous olive-like carbon toward universal high-performance alkali (Li, Na, K)-ion storage. *Carbon*. 2021;174:317-324.

4. Yan D, Zhang J, Xiong D, et al. Boosting chem-insertion and phys-adsorption in S/N co-doped porous carbon nanospheres for high-performance symmetric Li-ion capacitors. *J Mater Chem A*. 2020;8(23):11529-11537.

5. Yu L, Liu J, He S, et al. N-doped rGO/C@Si composites using sustainable chitosan as the carbon source for lithium-ion batteries. *Appl Surf Sci*. 2020;501:144136.

6. Zhang S, Qiu L, Zheng Y, et al. Rational design of core-shell ZnTe@N-doped carbon nanowires for high gravimetric and volumetric alkali metal ion storage. *Adv Funct Mater*. 2021;31(3):2006425.

7. Gomez-Martin A, Martinez-Fernandez J, Ruttert M, Winter M, Placke T, Ramirez-Rico J. An electrochemical evaluation of nitrogen-doped carbons as anodes for lithium ion batteries. *Carbon*. 2020;164:261-271.

8. Kleiner K, Jakes P, Scharner S, Liebau V, Ehrenberg H. Changes of the balancing between anode and cathode due to fatigue in commercial lithium-ion cells. *J Power Sources*. 2016;317:25-34.

9. Kleiner K, Ehrenberg H. Challenges considering the degradation of cell components in commercial lithium-ion cells: a review and evaluation of present systems. *Top Curr Chem*. 2017;375(3):54.

10. Li Y, Chen M, Liu B, Zhang Y, Liang X, Xia X. Heteroatom doping: an effective way to boost sodium ion storage. *Adv Energy Mater*. 2020;10(27):2000927.

11. Vesel A, Zaplotnik R, Primc G, Mozetic M. A review of strategies for the synthesis of N-doped graphene-like materials. *Nanomaterials*. 2020;10(11):2286.

12. Pan H. Graphitic carbon nitride nanotubes as Li-ion battery materials: a first-principles study. *J Phys Chem C*. 2014; 118(18):9318-9323.

13. Veith GM, Baggetto L, Adamczyk LA, et al. Electrochemical and solid-state lithiation of graphitic C_3N_4. *Chem Mater*. 2013;25(3):503-508.

14. Chen J, Mao Z, Zhang L, et al. Nitrogen-deficient graphitic carbon nitride with enhanced performance for lithium ion battery anodes. *ACS Nano*. 2017;11(12):12650-12657.

15. Tang Y, Wang X, Chen J, Wang X, Wang D, Mao Z. PVP-assisted synthesis of g-C_3N_4-derived N-doped graphene with tunable interplanar spacing as high-performance lithium/sodium ions battery anodes. *Carbon*. 2021;174:98-109.

16. Tang Y, Wang X, Chen J, Wang X, Wang D, Mao Z. Templated transformation of g-C_3N_4 nanosheets into nitrogen-doped hollow carbon sphere with tunable nitrogen-doping properties for application in Li-ions batteries. *Carbon*. 2020;168:458-467.

17. Yu YX. Can all nitrogen-doped defects improve the performance of graphene anode materials for lithium-ion batteries? *Phys Chem Chem Phys*. 2013;15(39):16819-16827.

18. Hankel M, Ye DL, Wang LZ, Searles DJ. Lithium and sodium storage on graphitic carbon nitride. *J Phys Chem C*. 2015;119(38):21921-21927.

19. Ferrari AC, Meyer JC, Scardaci V, et al. Raman spectrum of graphene and graphene layers. *Phys Rev Lett*. 2006;97(18):187401.

20. Yang R, Yang Y, Chen X, Yang Q. A general strategy for antimony-based alloy nanocomposite embedded in Swiss-cheese-like nitrogen-doped porous carbon for energy storage. *Adv Funct Mater*. 2021;31(13):2009433.

21. Wang H, Zhang X, Xie J, et al. Structural distortion in graphitic-C$_3$N$_4$ realizing an efficient photoreactivity. *Nanoscale*. 2015;7(12): 5152-5156.

22. Li X, Zhang J, Shen L, et al. Preparation and characterization of graphitic carbon nitride through pyrolysis of melamine. *Appl Phys A*. 2009;94(2):387-392.

23. Berthold T, Castro CR, Winter M, et al. Tunable nitrogen-doped carbon nanoparticles from tannic acid and urea and their potential for sustainable soots. *ChemNanoMat*. 2017;3(5):311-318.

24. Bosilj M, Rustam L, Thomann R, Melke J, Fischer A, White RJ. Directing nitrogen-doped carbon support chemistry for improved aqueous phase hydrogenation catalysis. *Catal Sci Technol*. 2020;10(14):4794-4808.

25. Kruk M, Jaroniec M. Gas adsorption characterization of ordered organic-inorganic nanocomposite materials. *Chem Mater*. 2001;13(10):3169-3183.

26. Xiao X, Zou LL, Pang H, Xu Q. Synthesis of micro/nanoscaled metal-organic frameworks and their direct electrochemical applications. *Chem Soc Rev*. 2020;49(1):301-331.

27. Pender JP, Guerrera JV, Wygant BR, et al. Carbon nitride transforms into a high lithium storage capacity nitrogen-rich carbon. *ACS Nano*. 2019;13(8):9279-9291.

28. Kubota K, Shimadzu S, Yabuuchi N, et al. Structural analysis of sucrose-derived hard carbon and correlation with the electrochemical properties for lithium, sodium, and potassium insertion. *Chem Mater*. 2020;32(7):2961-2977.

29. Tao L, Yang Y, Wang H, et al. Sulfur-nitrogen rich carbon as stable high capacity potassium ion battery anode: performance and storage mechanisms. *Energy Storage Mater*. 2020;27:212-225.

30. Sui ZY, Wang C, Yang QS, et al. A highly nitrogen-doped porous graphene—an anode material for lithium ion batteries. *J Mater Chem A*. 2015;3(35):18229-18237.

31. Ai W, Jiang J, Zhu J, et al. Supramolecular polymerization promoted in situ fabrication of nitrogen-doped porous graphene sheets as anode materials for Li-Ion batteries. *Adv Energy Mater*. 2015;5(15):1500559.

32. Qie L, Chen WM, Wang ZH, et al. Nitrogen-doped porous carbon nanofiber webs as anodes for lithium ion batteries with a superhigh capacity and rate capability. *Adv Mater*. 2012;24(15):2047-2050.

33. Nan D, Huang ZH, Lv R, et al. Nitrogen-enriched electrospun porous carbon nanofiber networks as high-performance free-standing electrode materials. *J Mater Chem A*. 2014;2(46): 19678-19684.

34. Sun Y, Ning G, Qi C, et al. An advanced lithium ion battery based on a sulfur-doped porous carbon anode and a lithium iron phosphate cathode. *Electrochim Acta*. 2016;190:141-149.

35. Zhou C, Wang D, Yang H, et al. N, O co-doped urchin-like carbon microspheres as high-performance anode materials for lithium ion batteries. *Solid State Ion*. 2021;361:115562.

36. Zhan Y, Zhang B, Cao L, et al. Iodine doped graphene as anode material for lithium ion battery. *Carbon*. 2015;94:1-8.

37. Gao C, Feng J, Dai J, et al. Manipulation of interlayer spacing and surface charge of carbon nanosheets for robust lithium/sodium storage. *Carbon*. 2019;153:372-380.

38. He SA, Liu Q, Cui Z, et al. Red phosphorus anchored on nitrogen-doped carbon bubble-carbon nanotube network for highly stable and fast-charging lithium-ion batteries. *Small*. 2022;18(7):2105866.

39. Illa MP, Pathak AD, Sharma CS, Khandelwal M. Bacterial cellulose-polyaniline composite derived hierarchical nitrogen-doped porous carbon nanofibers as anode for high-rate lithium-ion batteries. *ACS Appl Energy Mater*. 2020;3(9): 8676-8687.

40. Zheng S, Luo Y, Zhang K, Liu H, Hu G, Qin A. Nitrogen and phosphorus co-doped mesoporous carbon nanosheets derived from bagasse for lithium-ion batteries. *Mater Lett*. 2021;290:129459.

41. Xing B, Zeng H, Huang G, et al. Magnesium citrate induced growth of noodle-like porous graphitic carbons from coal tar pitch for high-performance lithium-ion batteries. *Electrochim Acta*. 2021;376:138043.

42. Xing Z, Ju Z, Zhao Y, et al. One-pot hydrothermal synthesis of nitrogen-doped graphene as high-performance anode materials for lithium ion batteries. *Sci Rep*. 2016;6:26146.

43. Yuan CZ, Jiang YF, Wang Z, et al. Cobalt phosphate nanoparticles decorated with nitrogen-doped carbon layers as highly active and stable electrocatalysts for the oxygen evolution reaction. *J Mater Chem A*. 2016;4(21): 8155-8160.

44. Idrees M, Batool S, Kong J, et al. Polyborosilazane derived ceramics—nitrogen sulfur dual doped graphene nanocomposite anode for enhanced lithium ion batteries. *Electrochim Acta*. 2019;296:925-937.

45. He XL, Cai YQ, Zhao W, Zhuang QC, Ju ZC. Synthesis and electrochemical properties of nitrogen-doped porous carbon for lithium ion batteries. *J Phys Chem Solids*. 2020;147:109639.

46. Zhang JC, Qiu TS, Luan SY, Li HJ. Bounded non-linear covariance based ESPRIT method for noncircular signals in presence of impulsive noise. *Digit Signal Prog*. 2019;87: 104-111.

47. Tang Y, Wang X, Chen J, Wang X, Wang D, Mao Z. High-level pyridinic-N-doped carbon nanosheets with promising performances severed as Li-ion battery anodes. *Energy Technol*. 2020;8(9):2000361.

48. Zhang X, Zhu G, Wang M, Li J, Lu T, Pan L. Covalent-organic-frameworks derived N-doped porous carbon materials as anode for superior long-life cycling lithium and sodium ion batteries. *Carbon*. 2017;116:686-694.

49. Ruan J, Yuan T, Pang Y, et al. Nitrogen and sulfur dual-doped carbon films as flexible free-standing anodes for Li-ion and Na-ion batteries. *Carbon*. 2018;126:9-16.

50. Huang S, Li Z, Wang B, et al. N-doping and defective nanographitic domain coupled hard carbon nanoshells for

high performance lithium/sodium storage. *Adv Funct Mater.* 2018;28(10):1706294.

51. Wang D, Wang Z, Li Y, et al. In situ double-template fabrication of boron-doped 3D hierarchical porous carbon network as anode materials for Li- and Na-ion batteries. *Appl Surf Sci.* 2019;464:422-428.

52. Chen J, Mao Z, Zhang L, et al. Direct production of nitrogen-doped porous carbon from urea via magnesiothermic reduction. *Carbon.* 2018;130:41-47.

53. Prosini PP, Lisi M, Zane D, Pasquali M. Determination of the chemical diffusion coefficient of lithium in LiFePO$_4$. *Solid State Ion.* 2002;148(1-2):45-51.

54. Ding N, Xu J, Yao YX, et al. Determination of the diffusion coefficient of lithium ions in nano-Si. *Solid State Ion.* 2009;180(2-3):222-225.

55. Wang J, Polleux J, Lim J, Dunn B. Pseudocapacitive contributions to electrochemical energy storage in TiO$_2$ (anatase) nanoparticles. *J Phys Chem C.* 2007;111(40):14925-14931.

56. Augustyn V, Come J, Lowe MA, et al. High-rate electrochemical energy storage through Li$^+$ intercalation pseudocapacitance. *Nat Mater.* 2013;12(6):518-522.

SUPPORTING INFORMATION

Additional supporting information can be found online in the Supporting Information section at the end of this article.

How to cite this article: Tang Y, Chen J, Mao Z, Roth C, Wang D. High N-doped carbon with low graphitic-N content as anode material for enhanced initial Coulombic efficiency of lithium-ion batteries. *Carbon Energy.* 2023;5:e257. doi:10.1002/cey2.257